

Giant enhancement of second-harmonic generation from microcavity-integrated monolayer WS₂

Boyu Xu (徐博宇)^{1,2,3,†}, Xiao Xiong (熊霄)^{4,†}, Rui Niu (牛睿)¹, Guangyuan Qu (曲广媛)⁵, Chunhua Dong (董春华)^{1,2,3}, Guang-Can Guo (郭光灿)^{1,2,3}, and Xifeng Ren (任希锋)^{1,2,3*}

¹CAS Key Laboratory of Quantum Information, University of Science and Technology of China, Hefei 230026, China

²CAS Synergetic Innovation Center of Quantum Information & Quantum Physics, University of Science and Technology of China, Hefei 230026, China

³Hefei National Laboratory, University of Science and Technology of China, Hefei 230088, China

⁴State Key Laboratory for Mesoscopic Physics and Frontiers Science Center for Nano-optoelectronics, School of Physics, Peking University, Beijing 100871, China

⁵School of Physical Sciences, University of Science and Technology of China, Hefei 230026, China

[†]These authors contributed equally to this work.

*Corresponding author: renxf@ustc.edu.cn

Received November 4, 2024 | Accepted January 9, 2025 | Posted Online May 23, 2025

Transition metal dichalcogenide two-dimensional (2D) materials, exhibiting extraordinary properties absent in their bulk forms, have garnered significant attention in the field of nonlinear optical devices. However, the atomic-level thickness limits the light absorption, which makes the intensity of the nonlinear signal extremely weak. Through transferring monolayer WS₂ onto a silica microsphere, we report a giant second-harmonic generation (SHG) enhancement for approximately 1.46×10^7 times. The second-harmonic (SH) signal reaches 2.56 MHz pumped by a continuous wave laser of 2.5 mW. It is attributed to an enhancement of the pump laser due to the whispering gallery mode of the microsphere cavity. This work demonstrates the potential of microcavity-integrated monolayer 2D materials for nonlinear optics in integrated photonics.

Keywords: 2D materials; microcavity; nonlinear optics.

DOI: [10.3788/COL202523.061901](https://doi.org/10.3788/COL202523.061901)

1. Introduction

Two-dimensional (2D) transition metal dichalcogenides (TMDCs) are quantum materials that possess the merits of atomic thinness, direct bandgap, and spin-orbit coupling, thus holding promise for light-emitting and optoelectronic device applications^[1–6]. Moreover, their extraordinary nonlinear properties that are dependent on the number of layers have been extensively studied, establishing their indispensable role as building blocks in nonlinear optical devices^[7–16]. For example, the second-order nonlinear optical coefficient of monolayer tungsten disulfide (WS₂) is on the order of nanometers per volt^[8], at least 2 orders of magnitude higher than those of nonlinear crystals (e.g., lithium niobate)^[17]. However, being atomically thin results in a low harmonic signal of nanowatt^[8], limited by the efficiency of light absorption and emission. To enhance the intrinsically weak nonlinear optical processes, various nanostructures have been proposed to regulate the local density of optical states in layered TMDCs, including waveguides^[18–23], microcavities^[24–26], and metasurfaces^[27–32]. Among them,

whispering gallery mode (WGM) microcavities stand out for their ultrahigh quality (Q) factors and very small mode volumes, and they have found broad applications ranging from frequency conversion^[33–35] and quantum computing^[36–38] to optical sensing^[39]. In the WGM microcavity, the optical field propagates and undergoes total internal reflection at the inner surface. If the optical field returns to the starting point after one round trip with a phase difference that is an integer multiple of 2π , a standing wave mode is formed within the microcavity. In particular, transverse-electric WGMs offer the polarizability along the in-plane direction of layered TMDCs, perfectly aligned with their nonlinear susceptibility.

However, the integration of layered TMDCs with WGM microcavities has remained challenging. High-performance photonic integrated devices require the pick-and-place technique with high precision and uniformity when transferring layered, large-area TMDCs onto the on-chip WGM microcavities. Besides, any fragments introduced during the transfer process would inevitably decline the Q-factors of the microcavities, thus degrading the device performance. To address these challenges,

we develop the dry transfer method by dynamically heating the microcavities, which relies on the inherent van der Waals force and allows for manipulation of large-area TMDCs. As for the Q-factor control, the spherical microcavities formed through surface tension are good candidates, in which their atomically smooth surfaces assure the ultrahigh Q-factor (over 10^9 attainable)^[40].

In this work, we study microcavity-enhanced second-harmonic generation (SHG) in monolayer WS_2 . It is found that with a high-Q silica microsphere (MS), the second-harmonic (SH) signal generated by a continuous-wave (CW) laser is much stronger than that for a pulsed laser, reaching the generation rate of 2.74×10^6 cps at a pump power of 2.5 mW. The WGM resonance remarkably boosts the SHG process, leading to an enhancement factor of 1.46×10^7 compared to that in the bare monolayer. The TMDC-integrated MSs serve as a versatile platform for the fundamental studies of $\chi^{(2)}$ and $\chi^{(3)}$ nonlinear optical processes^[41]. Moreover, as movable scanning microprobes, they would promote applications including portable quantum light sources, Raman spectroscopy, imaging, and surface chemical analysis^[42].

2. Experiments and Methods

2.1. Experimental setup and SHG enhancement mechanism

The experimental setup is shown in Fig. 1(c). To match the cavity mode with a very narrow bandwidth, we choose a tunable continuous laser (Santec TSL-550) in the 1550 nm band as the pump light source. A portion of the input light's energy is amplified and directed into a periodically poled lithium niobate (PPLN) crystal to generate a laser whose wavelength exhibits synchronous variations with the pump light, enabling simultaneous characterization of the transmission spectra in both frequency bands. During the SH test, the output of the PPLN crystal is disconnected to prevent it from affecting the results. The pump light and generated SH signal are collected from the microcavity using a tapered fiber. The tapered fiber exhibits a minimum diameter of 1.6 μm and demonstrates transmission efficiencies of 88.1% at 1550 nm and 66.7% at 775 nm, respectively. In order to ensure the stability of experimental results, we cause the fiber and cavity to be in direct contact to achieve the overcoupling state, although this may reduce the loaded Q factor. The SH signal coupled by the fiber is separated from the pump light by a wavelength division

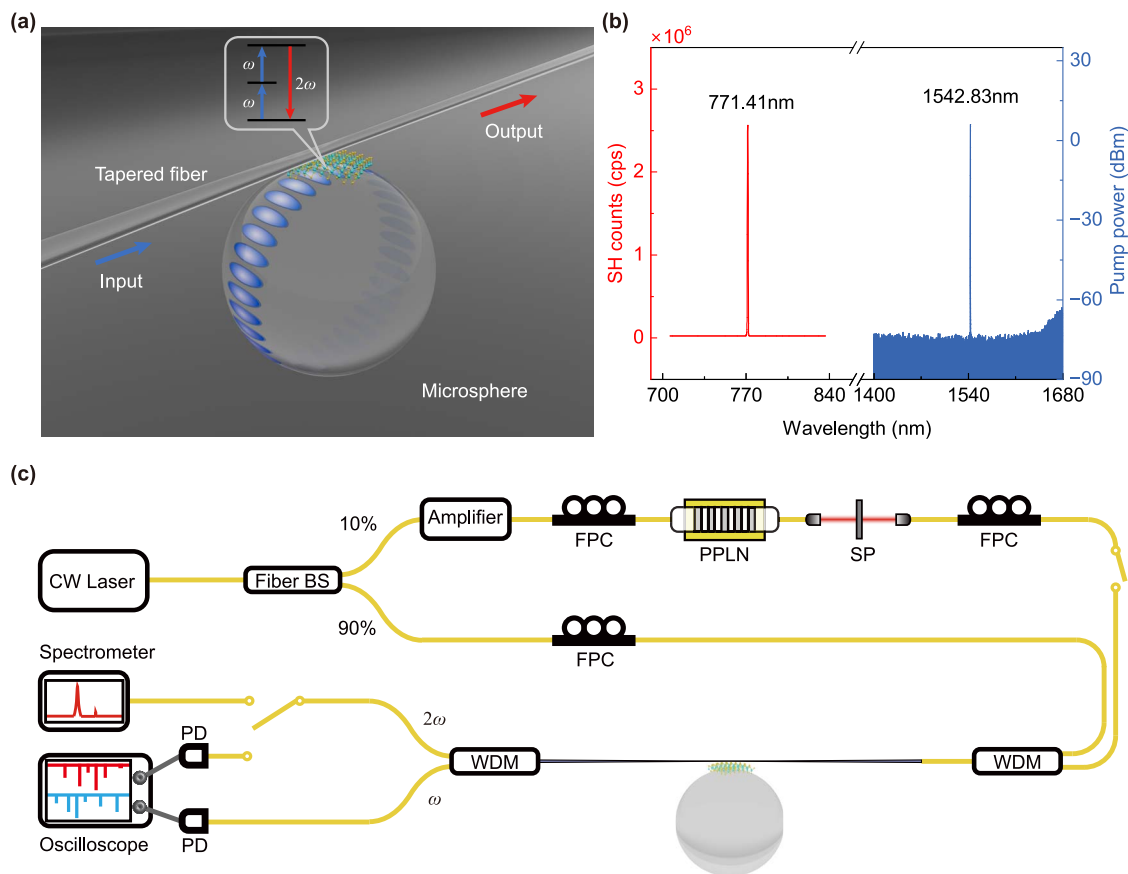


Fig. 1. (a) Schematic of SHG in monolayer WS_2 enhanced by the microsphere. The incident light and SH signal are coupled through a tapered fiber. (b) Measured spectra of the SH signal (red) as well as the pump laser (blue). (c) Schematic of experimental setup for measurement of SHG and transmission spectra. BS, beam splitter; FPC, fiber polarization controller; SP, 950 nm short pass filter; PD, photon detector; WDM, wavelength division multiplexer.

multiplexer (WDM) and measured using a spectrometer. The pump light is fed into the photodetector simultaneously to observe the transmission spectrum of the cavity in real time.

The SH intensity of monolayer WS₂ is mainly determined by its properties (second-order nonlinear susceptibility tensor) and the energy of the pump light. The monolayer WS₂ has P6₃/mmc crystal symmetry, which means it has a second-order nonlinear susceptibility tensor with nonzero elements $d_{yyy} = -d_{yxx} = -d_{xxy} = -d_{xyx}$ ^[8]. The polarization information of the SH signal reads

$$\begin{pmatrix} P_a(2\omega) \\ P_b(2\omega) \\ P_z(2\omega) \end{pmatrix} = 2\epsilon_0 \begin{pmatrix} d_{11} & \cdots & d_{16} \\ d_{21} & \cdots & d_{26} \\ d_{31} & \cdots & d_{36} \end{pmatrix} \begin{pmatrix} E_a(\omega)^2 \\ E_b(\omega)^2 \\ E_z(\omega)^2 \\ 2E_b(\omega)E_z(\omega) \\ 2E_a(\omega)E_z(\omega) \\ 2E_a(\omega)E_b(\omega) \end{pmatrix}, \quad (1)$$

where $E_i(\omega)$, $i = a, b, z$ are the components of the pump along the crystal orientations. Assuming that the absolute value of the nonzero elements of the tensor matrix is d , the components of the SH signal read

$$\begin{cases} P_a(2\omega) = -4\epsilon_0 d E_a(\omega) E_b(\omega) \\ P_b(2\omega) = -2\epsilon_0 d [E_a(\omega)^2 - E_b(\omega)^2] \\ P_z(2\omega) = 0 \end{cases} \quad (2)$$

Obviously, only the electric field within the material plane contributes to the SH signal. Fortunately, the MS cavity not only increases the energy of the light field but also provides the in-plane field, which makes it possible to effectively enhance the SHG of monolayer WS₂.

The light field of the fundamental mode is confined to a narrow and thin ring region near the equator of the MS as the schematic shown in Fig. 1(a). The fundamental modes possess extremely small mode volume and high energy density, which facilitates the light-matter interaction. The higher-order cavity modes with in-plane polarization can also enhance the SHG process. However, as the mode order increases, the number of nodal points of the optical field in the three directions of spherical coordinates increases, which causes the energy distribution of the optical field to spread, leading to a decrease in the enhancement effect. In theory, the 2D materials near the equator of the cavity can participate in the frequency-doubling process. Part of the energy of the light field is distributed outside the surface, which can excite the SH of monolayer WS₂. Figure 1(b) shows a typical SH and the corresponding pump spectra measured by an optical spectrum analyzer. The SH signal appears at 771.41 nm when pumped at 1542.83 nm. It is important to emphasize that there are many modes that can resonate with the microcavity, which reduces the limitation on the wavelength of the pump light source.

2.2. WS₂-integrated microcavity

In the experiment, the monolayer WS₂ (Six Carbon Tech.) is carefully transferred onto the surface of the silica MS made from single-mode fiber at telecom. In order to facilitate the subsequent transfer process, we choose polydimethylsiloxane (PDMS) as the sample base. During the transfer process, the glass slide holding the MS is positioned onto the heating plate. Meanwhile, the monolayer material slowly approaches the MS under the control of a piezo translation stage. Stop moving the material after contact with the surface of the MS and increase the temperature of the heating plate. In the process of gradual warming, the volume of the cavity will slowly expand to make its contact area with the material larger. Since PDMS is soft, the cavity will not be damaged by extrusion during the transfer process. When the temperature reaches 180°C, we slowly separate the sample from the MS, and the material in contact with the surface is transferred to the cavity due to van der Waals force. The whole transfer process is completed in a dry environment, which avoids the influence of the solution to the Q factor in the wet transfer. Compared with the single-layer discrete triangular single crystal grains, the continuous material does not need to be precisely located, and the transferred material area is larger.

Figure 2(a) shows the silica MS with a diameter of 52 μm. We conduct Raman spectroscopy tests at different positions on the surface of the cavity, and the results match those of monolayer WS₂, which demonstrates the effectiveness of the transfer method. The microcavity is fabricated by employing a high-power laser to melt the single-mode fiber at 1550 nm. Compared with other microstructures made by electron-beam lithography, the spherical cavity not only has a simpler fabrication process but also has good properties. By this method of melting standard optical fiber, we can easily fabricate microcavities with Q factors reaching up to the order of 10⁷. Due to the new material transfer technique, the modes of the cavity after transfer correspond well to those without transfer, and the Q factors decrease by 1 order of magnitude. On the one hand, dust and moisture in the air will attach to the microcavity and the 2D materials during the transfer process. The decrease in surface cleanliness leads to a reduction in the Q factor. On the other hand, during the transfer, the microcavity may experience slight deformation due to heating and pressure, resulting in a change in the Q factor of the microcavity modes. Figure 2(b) shows the typical transmission spectrum with different modes of the MS. Figure 2(c) presents a transmission spectrum of the cavity mode near 1546.2 nm, whose Q factor is up to 1.2 × 10⁶.

Distinct from other WGM microcavities (microrings, microdisks, and microtoroids), the spherical surface enables the cavity to fully contact the material during the transfer process, thereby increasing the transfer area. Such a large transfer area greatly increases the range of light-matter interaction, which is a major advantage of the MS compared to other structures supporting localized surface plasmons^[43–45]. The WGMs of the MS can propagate in a small volume near the surface, and the simulation of the electric field distribution is shown in Fig. 2(a). Some WGMs possess E-fields predominantly parallel to the plane of

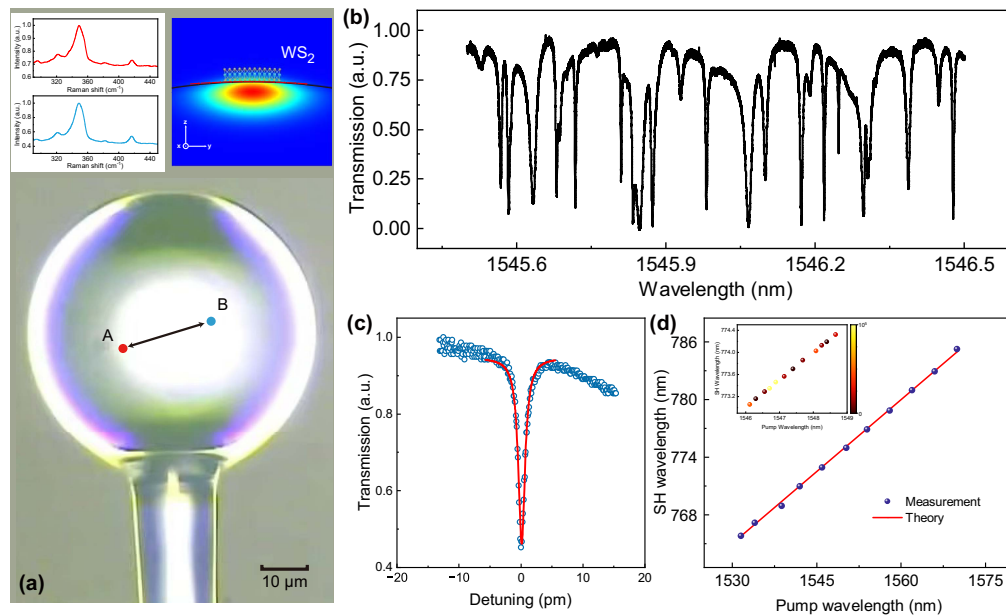


Fig. 2. (a) The CCD image of the microcavity in the x - y plane. We make Raman spectra measurements at positions A and B, and the results are shown in the insets (left). Inset figure (right) shows the simulation of electric field distribution of the microsphere with a monolayer WS₂ on its surface in the y - z plane. The red arrow represents the polarization direction of the electric field. The x -axis is the direction of the light field propagating. The two-dimensional material depicted in the figure is purely schematic, with an actual thickness of less than 1 nm. (b) Transmission spectrum of a microsphere without a material. (c) Transmission spectrum at 1546.2 nm. The Q factor of the mode reaches 1.2×10^6 . (d) SH wavelengths versus the corresponding pump wavelengths. The figure shows the measurement results for resonant modes near wavelengths with equal intervals. As the pump wavelength changes, the mode corresponding to the fundamental frequency also changes, causing the SH intensity to fluctuate. However, the SH wavelength remains half of the pump wavelength. Inset: experimental results at a smaller wavelength range. The color of the data point represents the intensity of the doubled frequency signal.

material to excite SHG of WS₂ monolayer film. Thanks to the large number of modes in the microcavity, the SH signals can be observed when the pump wavelength changes from 1530 to 1570 nm. The strengths of the signal are related to the resonance modes; therefore, at the same pump power, there is still a significant difference in SH power. Figure 2(d) presents the dependence between SH and pump wavelength, which clearly demonstrates a linear relationship with a slope of 0.5. Moreover, the inset in Fig. 2(d) shows the wavelength dependence in a smaller wavelength range, with the color of each data point representing the intensity of the SH signal. It should be noted that there are a large number of modes in the cavity that can excite the SHG, and it is not possible to measure at every resonant wavelength. Therefore, the inset only shows the data points with higher intensity. In addition, we conduct frequency-doubling tests on the MS cavity without monolayer WS₂, and no SH signal is observed when the pump wavelength resonates with the microcavity. The significant difference in the test results between the two cases indicates that the SH signals originate from the monolayer material.

3. Results

For monolayer materials at the non-enhancement case, the SH intensity of pulsed laser (MenloSystems TERA K15, bandwidth 72 nm) pumping is much greater than that of the CW laser

pumping under the same pump power (using a reflective optical system in the experiment) as shown in Figs. 3(a) and 3(b). The objective lens (Mitutoyo, M Plan NIR 20X) used in the experiment has a magnification of 20 times and a working distance of 20 mm. The experimental results of the microcavity enhanced case are opposite, which proves that the MS has the ability to greatly enhance the SHG of monolayer WS₂. In Fig. 3(c), the CW laser-pumped SH signal has a narrower bandwidth and higher intensity, which is much greater than the non-enhancement case. Due to the continuous laser possessing a very narrow bandwidth, basically all the energy was bound in the spherical cavity when the pump light resonated with the mode. As for the pulsed pumping case, there is no significant difference between the two cases, primarily because most of the laser energy does not resonate with the microcavity. Nevertheless, the energy of the pulsed light resonating with the microcavity modes causes some irregular peaks to appear in the spectrum.

Furthermore, the intensity dependence between the SH signal and incident light pumped at 1542.83 nm is indicated in Fig. 3(e). The Q factor of the WGM mode at 1542.83 nm reaches 1.12×10^6 . Experimentally, we achieve the maximum signal by optimizing the pump wavelength for each input power level. As the pump power increases, the intensity variation of the SH signals can be divided into three stages: A, B, and C. In stage A, the SH power is very low and remains essentially unchanged with the pump power, as there is little energy resonating with the microcavity. In stage B, the counts of SH rapidly increase

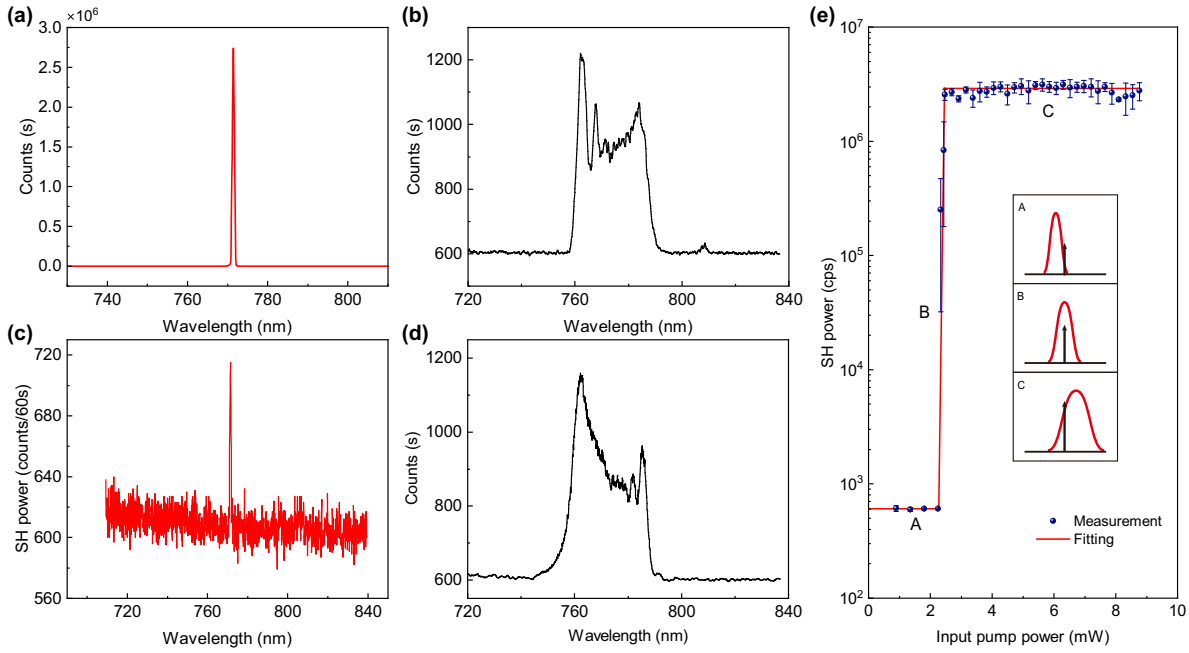


Fig. 3. (a), (b) Measured SH spectra of the cavity-enhanced monolayer WS_2 under CW laser input and pulse laser input, respectively. (c), (d) Measured SH spectra of the monolayer WS_2 under CW laser input and pulse laser input, respectively. (e) Dependence between SH power and input power for the same pump mode at 1542.83 nm. A–C represent different variation processes of SH power. Inset: schematic of the SHG process. The black arrows represent the pump lights. The red Lorentzian shapes represent the pump cavity modes.

to 2.56 MHz, and the conversion efficiency of SHG with a pump power of 2.5 mW comes up to $1.08 \times 10^{-7}/W$. At this point, the increase in pump energy causes thermal effects that lead to the broadening and redshift of the cavity mode, resulting in a significant increase in the proportion of resonating energy and a rapid rise in the SH power. In stage C, the SH signal remains stable near 3 MHz. On the one hand, the increase in pump power enhances the energy resonating within the microcavity. On the other hand, the continuous increase of the pump laser exacerbates thermal effects, causing a detuning between the pump wavelength and the cavity mode. Under the interplay of these two effects, the energy resonating in the cavity remains at a stable level, resulting in the SH power remaining essentially unchanged. In the non-enhancement case, the SHG exhibits an extremely low conversion efficiency of $7.42 \times 10^{-15}/W$ pumped by the CW laser at 1542.8 nm. The intensity of SH enhanced by the MS is improved by about 1.46×10^7 times compared with the non-enhanced case. Such a huge enhancement proves that the MS has the ability to improve the SHG of monolayer WS_2 . The intensity of the frequency-doubling signal remains sufficiently high to cater to a wide range of application scenarios.

4. Discussion and Conclusion

Even if the enhancement factor reaches 10^7 , a few aspects can be improved further. First, the light field energy is mainly distributed inside the spherical cavity, which results in only part of the energy participating in the excitation of the 2D material located on the surface. Due to the atomic thickness of the

monolayer WS_2 , it has little effect on the energy distribution in the microcavity as the simulation results shown in Fig. 4(a). A small increase in the number of material layers has no significant effect on the energy distribution but will lead to a decrease in the SH signal^[46]. When the material thickness is over 10 nm, the energy ratio of the material layer increases significantly, but this simultaneously leads to an escalation in energy dissipation, which results in a decrease in the Q factor of the cavity. Compared with multilayer cases, the monolayer material has the least influence on Q factor and the strongest SH signal. In future work, transferring a single layer of material inside a microcavity could significantly increase the energy involved in the nonlinear process, although this approach would greatly increase the difficulty of sample fabrication.

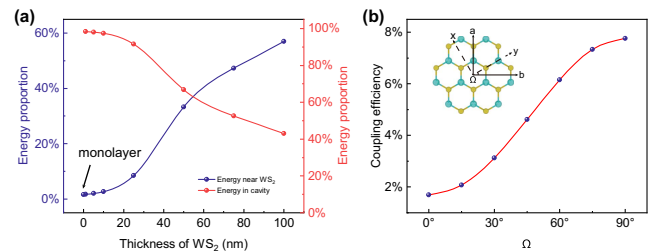


Fig. 4. (a) The effect of material thickness on energy distribution. As the thickness increases, the energy becomes more concentrated near the 2D material while the energy inside the cavity decreases. (b) The relationship between Ω and the coupling efficiency of the tapered fiber to the SH signal. Inset: demonstration of the angle (Ω) between the crystal orientations (x, y) and the coordinates (a, b).

Secondly, a tapered fiber of the 1550 nm band is used to couple with the cavity, which leads to a good coupling efficiency of the pump laser. However, the extraction efficiency of SH is low since the signal does not resonate with the cavity. Moreover, the coupling efficiency also depends on the angle Ω between the polarization of the pump light and the crystal direction. We estimated the collection efficiency of tapered fiber by COMSOL, and the result was from 1.7% to 7.8%, as shown in Fig. 4(b). Notably, we treated the photons emitted from the monolayer WS_2 as electric dipoles with in-plane orientation. Further enhancement of SHG may be achieved by the design of the coupling of two tapered fibers and double resonance^[33,47,48].

In conclusion, we experimentally enhance the SHG of a monolayer WS_2 using an MS cavity with a diameter of 52 μm . The high energy density of the WGM modes in the microcavity allows us to excite the SH process of monolayer WS_2 under the pump of a CW laser. Tuning the pump laser wavelength to match the cavity mode significantly improves the light-matter interactions in WS_2 , which enhances the intensity of the SH signal. A giant SH enhancement of about 1.46×10^7 was observed to be pumped by a CW 1550 nm laser. Further SH enhancements can be achieved through improving the technique of material transfer or realizing the double resonance. Such a huge enhancement shows that the WGM microcavity is a promising method for investigating the nonlinearity of 2D materials. Furthermore, optical devices integrating microcavities and 2D materials with ultrahigh $\chi^{(2)}$ will become a new platform for investigating micro-nano nonlinear optics and even for the preparation of quantum light sources. During the preparation of this paper, we noticed that another paper similar to our work has been published^[41]. Both works discuss the potential of cavity-enhanced 2D materials. However, our work focuses more on the enhancement of 2D materials under the condition of a single resonance.

Acknowledgements

This work was supported by the National Key Research and Development Program of China (No. 2022YFA1204704), the Innovation Program for Quantum Science and Technology (Nos. 2021ZD0301500 and 2021ZD0303200), the National Natural Science Foundation of China (Nos. 62061160487, T2325022, U23A2074, 12104440, and 12293051), the CAS Project for Young Scientists in Basic Research (No. YSBR-049), and the Key Research and Development Program of Anhui Province (No. 2022b1302007). This work was partially carried out at the USTC Center for Micro and Nanoscale Research and Fabrication.

References

- I. H. R. Gutiérrez, N. Perea-López, A. L. Elías, *et al.*, "Extraordinary room-temperature photoluminescence in triangular WS_2 monolayers," *Nano Lett.* **13**, 3447 (2013).
- P. Tonndorf, R. Schmidt, P. Böttger, *et al.*, "Photoluminescence emission and Raman response of monolayer MoS_2 , MoSe_2 , and WSe_2 ," *Opt. Express* **21**, 4908 (2013).
- W. Shi, M.-L. Lin, Q.-H. Tan, *et al.*, "Raman and photoluminescence spectra of two-dimensional nanocrystallites of monolayer WS_2 and WSe_2 ," *2D Mater.* **3**, 025016 (2016).
- X. Qi, T. W. Lo, D. Liu, *et al.*, "Effects of gap thickness and emitter location on the photoluminescence enhancement of monolayer MoS_2 in a plasmonic nanoparticle-film coupled system," *Nanophotonics* **9**, 2097 (2020).
- K. F. Mak and J. Shan, "Photonics and optoelectronics of 2D semiconductor transition metal dichalcogenides," *Nat. Photonics* **10**, 216 (2016).
- Q. H. Wang, K. Kalantar-Zadeh, A. Kis, *et al.*, "Electronics and optoelectronics of two-dimensional transition metal dichalcogenides," *Nat. Nanotechnol.* **7**, 699 (2012).
- B. Guo, Q.-L. Xiao, S.-H. Wang, *et al.*, "2D layered materials: synthesis, nonlinear optical properties, and device applications," *Laser Photon. Rev.* **13**, 1800327 (2019).
- C. Janisch, Y. Wang, D. Ma, *et al.*, "Extraordinary second harmonic generation in tungsten disulfide monolayers," *Sci. Rep.* **4**, 5530 (2014).
- Y. Li, Y. Rao, K. F. Mak, *et al.*, "Probing symmetry properties of few-layer MoS_2 and h-BN by optical second-harmonic generation," *Nano Lett.* **13**, 3329 (2013).
- N. Kumar, S. Najmaei, Q. Cui, *et al.*, "Second harmonic microscopy of monolayer MoS_2 ," *Phys. Rev. B* **87**, 161403 (2013).
- M. Wang, D. Li, K. Liu, *et al.*, "Nonlinear optical imaging, precise layer thinning, and phase engineering in MoTe_2 with femtosecond laser," *ACS Nano* **14**, 11169 (2020).
- K. L. Seyler, J. R. Schaibley, P. Gong, *et al.*, "Electrical control of second-harmonic generation in a WSe_2 monolayer transistor," *Nat. Nanotechnol.* **10**, 407 (2015).
- F. Yi, M. Ren, J. C. Reed, *et al.*, "Optomechanical enhancement of doubly resonant 2D optical nonlinearity," *Nano Lett.* **16**, 1631 (2016).
- W.-T. Hsu, Z.-A. Zhao, L.-J. Li, *et al.*, "Second harmonic generation from artificially stacked transition metal dichalcogenide twisted bilayers," *ACS Nano* **8**, 2951 (2014).
- H. Liu, Y. Li, Y. S. You, *et al.*, "High-harmonic generation from an atomically thin semiconductor," *Nat. Phys.* **13**, 262 (2017).
- C. T. Le, D. J. Clark, F. Ullah, *et al.*, "Nonlinear optical characteristics of monolayer MoSe_2 ," *Ann. Phys. Lpz.* **528**, 551 (2016).
- R. W. Boyd, *Nonlinear Optics* (Academic Press, 2020).
- H. Chen, V. Corbaliou, A. S. Solntsev, *et al.*, "Enhanced second-harmonic generation from two-dimensional MoSe_2 on a silicon waveguide," *Light Sci. Appl.* **6**, e17060 (2017).
- G. Q. Ngo, E. Najafidehaghani, Z. Gan, *et al.*, "In-fibre second-harmonic generation with embedded two-dimensional materials," *Nat. Photonics* **16**, 769 (2022).
- B. Jiang, Z. Hao, Y. Ji, *et al.*, "High-efficiency second-order nonlinear processes in an optical microfiber assisted by few-layer GaSe," *Light Sci. Appl.* **9**, 63 (2020).
- Y. Zuo, W. Yu, C. Liu, *et al.*, "Optical fibres with embedded two-dimensional materials for ultrahigh nonlinearity," *Nat. Nanotechnol.* **15**, 987 (2020).
- Z. Hao, B. Jiang, Y. Ma, *et al.*, "Broadband and continuous wave pumped second-harmonic generation from microfiber coated with layered GaSe crystal," *Opto-Electron. Adv.* **6**, 230012 (2023).
- J. Xie, X. Cheng, G. Xue, *et al.*, "Critical-layered MoS_2 for the enhancement of supercontinuum generation in photonic crystal fibre," *Adv. Mater.* **36**, 2403696 (2024).
- T. K. Fryett, K. L. Seyler, J. Zheng, *et al.*, "Silicon photonic crystal cavity enhanced second-harmonic generation from monolayer WSe_2 ," *2D Mater.* **4**, 015031 (2016).
- L. Zhang, R. Gogna, W. Burg, *et al.*, "Photonic-crystal exciton-polaritons in monolayer semiconductors," *Nat. Commun.* **9**, 713 (2018).
- J. Shi, X. Wu, K. Wu, *et al.*, "Giant enhancement and directional second harmonic emission from monolayer WS_2 on silicon substrate via Fabry-Pérot micro-cavity," *ACS Nano* **16**, 13933 (2022).
- J. Shi, W.-Y. Liang, S. S. Raja, *et al.*, "Plasmonic enhancement and manipulation of optical nonlinearity in monolayer tungsten disulfide," *Laser Photonics Rev.* **12**, 1800188 (2018).

28. Y. Ding, C. Wei, H. Su, *et al.*, “Second harmonic generation covering the entire visible range from a 2D material–plasmon hybrid metasurface,” *Adv. Opt. Mater.* **9**, 2100625 (2021).
29. N. Bernhardt, K. Koshelev, S. J. White, *et al.*, “Quasi-BIC resonant enhancement of second-harmonic generation in WS₂ monolayers,” *Nano Lett.* **20**, 5309 (2020).
30. F. J. Löchner, A. George, K. Koshelev, *et al.*, “Hybrid dielectric metasurfaces for enhancing second-harmonic generation in chemical vapor deposition grown MoS₂ monolayers,” *ACS Photonics* **8**, 218 (2020).
31. Z.-K. Zhou, H.-F. Xu, Y. Yu, *et al.*, “Giant nonlinear response of monolayer induced by optimal field-enhancement gain mode on the surface of hyperbolic metamaterials,” *Laser Photonics Rev.* **15**, 2100281 (2021).
32. Y. Deng, Z. Shi, Y. Zheng, *et al.*, “Highly efficient ultraviolet third-harmonic generation in an isolated thin Si meta-structure,” *Adv. Sci.* **11**, 2404094 (2024).
33. X. Guo, C.-L. Zou, and H. X. Tang, “Second-harmonic generation in aluminum nitride microrings with 2500%/w conversion efficiency,” *Optica* **3**, 1126 (2016).
34. J. Fürst, D. Strekalov, D. Elser, *et al.*, “Naturally phase-matched second-harmonic generation in a whispering-gallery-mode resonator,” *Phys. Rev. Lett.* **104**, 153901 (2010).
35. J. Lu, J. B. Surya, X. Liu, *et al.*, “Periodically poled thin-film lithium niobate microring resonators with a second-harmonic generation efficiency of 250,000%/w,” *Optica* **6**, 1455 (2019).
36. B.-Y. Xu, L.-K. Chen, J.-T. Lin, *et al.*, “Spectrally multiplexed and bright entangled photon pairs in a lithium niobate microresonator,” *Sci. China Phys. Mech. Astron.* **65**, 294262 (2022).
37. X. Guo, C.-L. Zou, C. Schuck, *et al.*, “Parametric down-conversion photon-pair source on a nanophotonic chip,” *Light Sci. Appl.* **6**, e16249 (2017).
38. T. J. Steiner, J. E. Castro, L. Chang, *et al.*, “Ultrabright entangled-photon-pair generation from an AlGaAs-on-insulator microring resonator,” *PRX Quantum* **2**, 010337 (2021).
39. X. Jiang, A. J. Qavi, S. H. Huang, *et al.*, “Whispering-gallery sensors,” *Matter* **3**, 371 (2020).
40. S. Spillane, T. Kippenberg, and K. Vahala, “Ultralow-threshold Raman laser using a spherical dielectric microcavity,” *Nature* **415**, 621 (2002).
41. S. Fujii, N. Fang, D. Yamashita, *et al.*, “van der Waals decoration of ultrahigh-Q silica microcavities for $\chi^{(2)}$ – $\chi^{(3)}$ hybrid nonlinear photonics,” *Nano Lett.* **24**, 4209 (2024).
42. W. Mao, Y. Li, X. Jiang, *et al.*, “A whispering-gallery scanning microprobe for Raman spectroscopy and imaging,” *Light Sci. Appl.* **12**, 247 (2023).
43. Z. Wang, Z. Dong, Y. Gu, *et al.*, “Giant photoluminescence enhancement in tungsten-diselenide–gold plasmonic hybrid structures,” *Nat. Commun.* **7**, 11283 (2016).
44. Z. Wang, Z. Dong, H. Zhu, *et al.*, “Selectively plasmon-enhanced second-harmonic generation from monolayer tungsten diselenide on flexible substrates,” *ACS Nano* **12**, 1859 (2018).
45. X. Han, K. Wang, P. D. Persaud, *et al.*, “Harmonic resonance enhanced second-harmonic generation in the monolayer WS₂–Ag nanocavity,” *ACS Photonics* **7**, 562 (2020).
46. H. Zeng, G.-B. Liu, J. Dai, *et al.*, “Optical signature of symmetry variations and spin-valley coupling in atomically thin tungsten dichalcogenides,” *Sci. Rep.* **3**, 1608 (2013).
47. X.-Z. Qi and X.-F. Ren, “Enhancement of the second harmonic generation from monolayer WS₂ coupled with a silica microsphere,” *Chin. Phys. B* **31**, 104203 (2022).
48. X. Zhang, Q.-T. Cao, Z. Wang, *et al.*, “Symmetry-breaking-induced nonlinear optics at a microcavity surface,” *Nat. Photonics* **13**, 21 (2019).